Proceedings of the ASME 2017 Conference on Smart Materials, Adaptive Structures and Intelligent Systems
SMASIS2017
September 18-20, 2017, Snowbird, UT, USA

SMASIS2017-3810

EXPLORING THE DYNAMIC CHARACTERISTICS OF DEGREE-4 VERTEX ORIGAMI METAMATERIALS

Yutong Xia, Hongbin Fang*, K.W. Wang

Department of Mechanical Engineering
University of Michigan
Ann Arbor, MI 48105, USA

ABSTRACT

Origami-inspired mechanical metamaterials could exhibit extraordinary properties that originate almost exclusively from the intrinsic geometry of the constituent folds. While most of current state of the art efforts have focused on the origami's static and quasi-static scenarios, this research explores the dynamic characteristics of degree-4 vertex (4-vertex) origami folding. Here we characterize the mechanics and dynamics of two 4-vertex origami structures, one is a stacked Miura-ori (SMO) structure with structural bistability, and the other is a stacked single-collinear origami (SSCO) structure with locking-induced stiffness jump; they are the constituent units of the corresponding origami metamaterials. In this research, we theoretically model and numerically analyze their dynamic responses under harmonic base excitations. For the SMO structure, we use a third-order polynomial to approximate the bistable stiffness profile, and numerical simulations reveal rich phenomena including small-amplitude intrawell, large-amplitude interwell, and chaotic oscillations. Spectrum analyses reveal that the quadratic and cubic nonlinearities dominate the intrawell oscillations and interwell oscillations, respectively. For the SSCO structure, we use a piecewise constant function to describe the stiffness jump, which gives rise to a frequency-amplitude response with hardening nonlinearity characteristics. Mainly two types of oscillations are observed, one with small amplitude that coincides with the linear scenario because locking is not triggered, and the other with large amplitude and significant nonlinear characteristics. The method of averaging is adopted to analytically predict the piecewise stiffness dynamics. Overall, this research bridges the gap between the origami quasi-static mechanics and origami folding dynamics, and paves the way for further dynamic applications of origami-based structures and metamaterials.

1. INTRODUCTION

Origami, an ancient art of paper folding, has gained new leaf of life recently, as its principles have not only been explored in mathematics and aesthetics, but also shed light on design and manufacturing of complex three-dimensional (3D) structures with profuse functionalities out of two-dimensional (2D) materials. Since origami folding possesses the property of scale-independence, various applications in a diverse range of scales can be expected, such as nano-scaled DNA origami [1], micro-scaled biomedical devices [2,3], macro-scaled printable robots [4–7], sandwich panels [8], actuators [9], as well as large-scaled aerospace [10] and architecture elements [11]. Recently origami also demonstrated its value in the development of mechanical metamaterials with extraordinary properties originated from folding, such as auxetic effect [12–14], reprogrammable stiffness [15], locking and stiffness jump [14,16], multi-stability [17,18], as well as high stiffness yet high reconfigurability [19] and recoverable collapse [20].

Despite the significant research progress on the static and quasi-static characteristics of origami structures, their dynamics features have not been systematically explored. On one hand, a dynamic folding process may be necessary or unavoidable when employing origami structures in various applications. On the other hand, origami structures could exhibit beneficial dynamic characteristics that hold promising potential in engineering. For example, previous researches [21–23] have demonstrated that the geometry-induced nonlinear and quasi-zero stiffness of origami structures can be utilized for vibration and impact mitigation. Nevertheless, a rigorous and comprehensive framework to investigate the origami dynamics is still lacking. Therefore, the goal of this paper is to advance the state of art through exploring the dynamic characteristics of two 4-vertex origami structures, one is a stacked Miura-ori

* Address all correspondence to this author: hongbinf@umich.edu

(SMO) structure with structural bistability, and the other is a stacked single-collinear origami (SSCO) structure with locking-induced stiffness jump.

The SMO structure is composed of two Miura-ori cells [12]. Miura-ori cell is the simplest degree-4 vertex pattern with flat-foldability and a pair of single-collinear creases. By stacking two Miura-ori cells (Figure 1(a)) with certain geometry constraints, a stacked flat-foldable Miura-ori unit can be constructed (Figure 1(b)). The thick lines represent the creases connecting cell A and cell B. When applying appropriate bending stiffness at certain creases, the unit could exhibit bistability, i.e., the structure could stay at two different configurations without external aid [24]. Bistability is a kind of strong nonlinearity with rich dynamics, some of which could be implemented for performance enhancement in various applications [25], such as energy harvesting [26], motion amplification [27,28], and vibration isolation [29]. However, despite its potential, the exploration of bistable dynamics in origami structures has never been pursued.

The SSCO structure is constructed by connecting two single-collinear cells, as shown in Figure 2. Single-collinear cell is also a degree-4 vertex pattern, which possesses fewer geometry constraints than Miura-ori [14,30]. The single-collinear cell loses the flat-foldability, i.e., folding of the cell will stop at a specific configuration without additional locker elements (e.g., active locking hinges [2,31] and shape-memory materials [32]) but due to origami facet-binding [14,16]. Such self-locking could be programmed by harnessing intrinsic geometry of single-collinear cells in a wide design space [16]. If assigning stiffness at certain creases, self-locking will give rise to a sudden jump of the structural stiffness and generate a piecewise stiffness profile. Piecewise stiffness has been demonstrated to be useful in vibration isolation and absorption [33,34]. However, in the origami field, the dynamic effects of self-locking and locking-induced piecewise stiffness have never been studied.

In this paper, instead of simplifying the origami structures into linkage systems, we fabricate "real" rigid-foldable origami prototypes. We perform compression tests on the prototypes to obtain the corresponding force-displacement profiles. In the experiments, the SMO structure shows clear bistability, and the stiffness of the SSCO structure exhibits significant jump phenomenon. Based on the measured profiles, analytical force-displacement curves of the SMO and SSCO structures can be approximated, which are used to establish equivalent dynamic model and serve the basis of dynamical investigation.

Numerical simulations on the two structures reveal rich dynamics that has never been reported. For the SMO structure, under harmonic base excitation, two distinct types of responses are observed: small-amplitude intrawell oscillations and large-amplitude interwell oscillations. Transmissibility analyses further indicate that the quadratic nonlinearity dominates the intrawell responses, while the cubic nonlinearity dominates the interwell responses. These nonlinearities are the origins of complex dynamics including subharmonic oscillations and chaotic oscillations.

For the SSCO structure, method of averaging [33] is applied to analyze the responses under harmonic base excitation. Two types of oscillations are inferred from the analytical results, one with small amplitude and close to the corresponding linear system's response, and the other with large amplitude. Numerical simulation is also performed to verify the analytical predictions.

This paper is organized as follows. Section 2 introduces the geometric design, folding kinematics, and mechanical properties of the SMO and SSCO structures. Section 3 presents the numerical analysis on the SMO structure's dynamics. In Section 4, we use the method of averaging to analyze the SSCO structure's dynamics, and verify the analytical results via numerical simulations. A brief summary is presented in Section 5.

2. GEOMETRY, KINEMATICS AND MECHANICS OF ORIGAMI STRUCTURES

2.1. Geometry and kinematics of the SMO structure

The SMO structure consists of two Miura-ori cells. Miura-ori is a special kind of degree-4 vertex pattern with a pair of collinear creases and reflectional symmetry about these creases. A Miura-ori cell can be described by three parameters: the length of adjacent creases (a,b) and the angle between them γ (Figure 1(a)). In what follows, subscripts 'A' and 'B' are used to identity the bottom cell A and the top cell B, respectively. With the rigid-foldability assumption, Miura-ori cell possesses a single degree-of-freedom (DOF) for folding. Folding of the Miura-ori cells could be described by the dihedral angles θ_A and θ_B between the facets and the $x-y$ plane (Figure 1(b)). To ensure kinematic compatibility, the following geometry constraints have to be satisfied [12] when connecting the two cells together

$$b_A = b_B = b,\ \frac{\cos(\gamma_B)}{\cos(\gamma_A)} = \frac{a_A}{a_B}, \tag{1}$$

$$\theta_B = \cos^{-1}(\cos(\theta_A)\frac{\tan(\gamma_A)}{\tan(\gamma_B)}). \tag{2}$$

In Eq. (2), for each θ_B two roots of θ_A with the same value but opposite signs can be obtained (with the only exception at $\theta_A = 0$). For clarity, the configurations corresponding to $\theta_A \in (0,\ \pi/2)$ and $\theta_A \in (-\pi/2,\ 0)$ are defined as nested-in and bulged-out, respectively (Figure 1(c) and (d)). This non-unique relationship between θ_A and θ_B, i.e., the non-unique configurations with respect to a given state of the top cell, is the geometry origin of the bistability in the SMO structure. With θ_A and θ_B, the dihedral angles between adjacent facets ρ_{ki} $(k = A, B;\quad i = 1,2,3,4)$ can be determined [12,14].

2.2. Geometry and kinematics of the SSCO structure

The SSCO structure consists of two single-collinear cells. Each single-collinear cell has a pair of collinear creases (Figure 2(a)), i.e., the four sector angles satisfy the following relation:

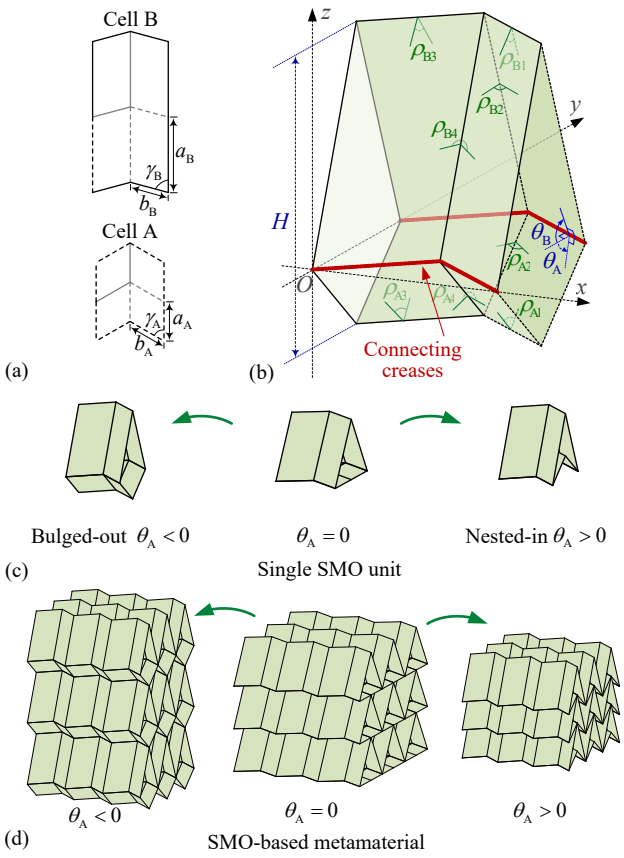

FIGURE 1. (a) The constituent top and bottowm Miura-ori cells. (b) The SMO structure, where the dihedral angles are denoted. (c) Three configurations of the SMO structure. (d) SMO-based mechanical metamaterial, shown in the bulged-out, an intermediate, and the nested-in configurations.

$$\alpha_{i1}+\alpha_{i2}=\alpha_{i3}+\alpha_{i4}=\pi,\quad i=A,B \tag{3}$$

Hence an SC cell can be determined by two sector angles $(\alpha_{i1},\alpha_{i4})=(\alpha_i,\beta_i)$ together with the lengths of a pair of adjacent creases (a_i,b_i). Similarly, the subscript 'i' could take 'A' or 'B' , indicating the bottom cell A or the top cell B, respectively.

Folding of the single-collinear cell is also a single DOF motion. It can be described by dihedral angles ρ_i $(i=1,2,3,4)$ between adjacent facets (Figure 2(b)) [14]. To connect two single-collinear cells together, the following geometric constraints have to be satisfied [14]

$$b_B=b_A,\ \frac{a_B}{a_A}=\frac{\cos(\alpha_A)}{\cos(\alpha_B)},\ \frac{\cos(\alpha_A)}{\cos(\alpha_B)}=\frac{\cos(\beta_A)}{\cos(\beta_B)},$$
$$\theta_B=\arcsin\sqrt{\frac{\cos^2\alpha_A+\cos^2\alpha_B\left(\sin^2\alpha_A\sin^2\theta_{A1}-1\right)}{\sin^2\alpha_B\cos^2\alpha_A}}. \tag{4}$$

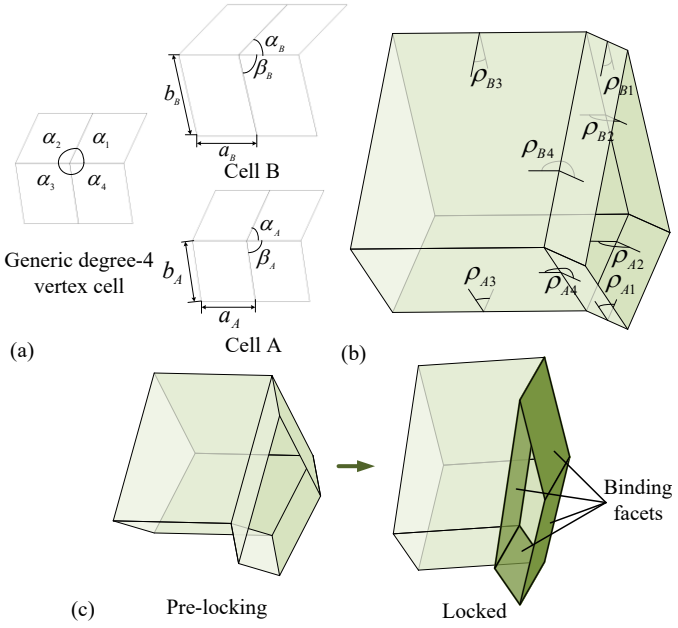

Figure 2. (a) A generic 4-vertex origami cell, and the consitutent top and bottom single-collinear origami cells. (b) The SSCO structure, where the diherdal angles are denoted. (c) The pre-locking and locked cnfigurations of the SSCO structure, where the binded facets are in dack color.

The SSCO structure remains a single DOF for folding. However, The SSCO structure cannot be folded flat but will stop at a specific configuration because two facets of cell A and two facets of cell B will bind simultaneously (Figure 2(c)).

2.3. Prototype and static tests of the SMO structure

An SMO structure prototype is fabricated in this research, (Figure 3(a)). The origami facets are made of water-jet-cut stainless steel sheet of thickness 0.25mm. By pasting the facets with plastic films of thickness 0.13mm, a Miura-ori cell prototype can be obtained. We attach 0.01mm-thick pre-bent spring-steel strips at certain creases to generate folding stiffness. We then further connect two Miura-ori cells into an SMO structure prototype with plastic film. In order to connect the prototype on the universal testing machine and shaker, 3D-printed connectors are screwed on the rectangular steel plates (Figure 3(b)). Such installation ensures the free folding the SMO structure, and meanwhile, external forces or displacements can be effectively transmitted to the SMO structure.

We perform five compression tests on the prototype, and the averaged force-displacement curve (solid curve) as well as the standard deviation (shaded band) is plotted in Figure 4. The SMO prototype shows obvious bistability during the tests, manifesting as two stable configurations u_1 and u_2 (i.e., the intersection points between the force-displacement curve and

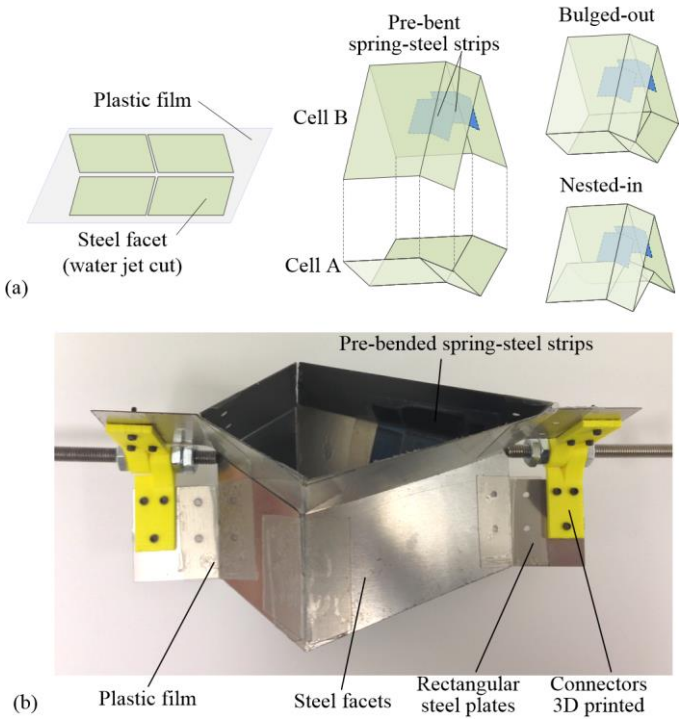

FIGURE 3. (a) Fabrication of the SMO structure. (b)Photo of the SMO prototype. The SMO structure is connected with 3D-printed connectors.

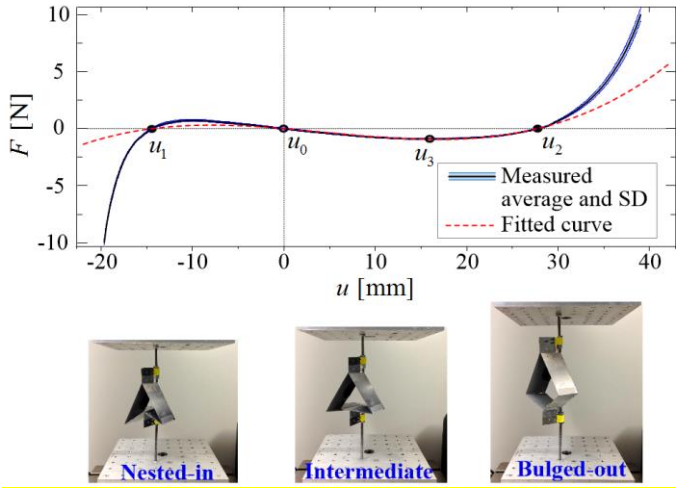

FIGURE 4. Measured and fitted force-displacement curves of the SMO structure prototype. Photos of the pototype at the nested-in, an intermediate, and the bulged-out configurations are given.

the horizontal axis with positive slope), an unstable configuration u_0 (i.e., the intersection point between the force-displacement curve and the horizontal axis with negative slope), and negative slopes between two stable configurations. For convenience, the unstable equilibrium u_0 is set as the origin of u in the following studies.

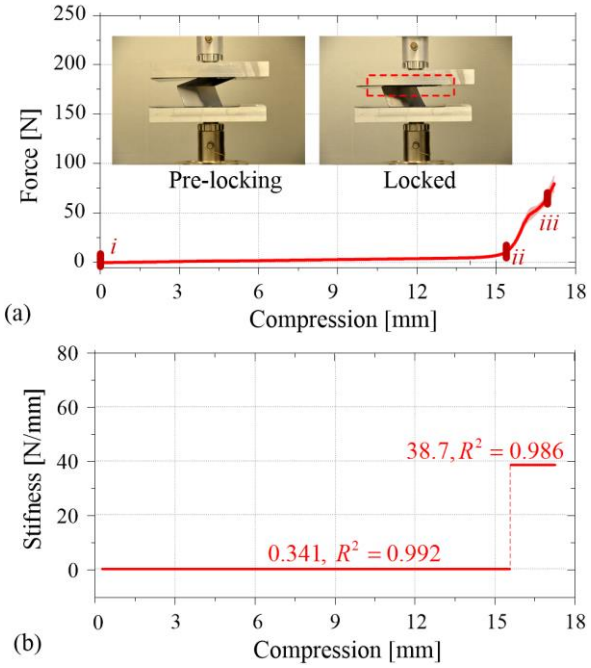

FIGURE 5. (a) Measured force-displacement curve of the SSCO structure prototype. Insets display the photos of the prototype before and after self-locking. (b) Approximated stiffness of the structure obtained through linear regression, the stiffness values and the coefficient of determination (R^2) are given.

2.4. Prototype and static tests of the SSCO structure

Through similar approaches as stated in Section 2.3 we fabricate an SSCO structure prototype. Here we also attach 0.01mm-thick pre-bent spring-steel stripes at the creases to generate folding stiffness. Five compression tests are performed on the SSCO structure to get the force-displacement curve (solid curve) and the standard deviation (shaded band), shown in Figure 5(a). It reveals that the curve is composed of two segments with significantly different slopes. Linear regression on each curve segment gives rise to the corresponding stiffness of the SSCO structure (Figure 5(b)). At the beginning stage of compression, the structural stiffness is low, which originates from the bending of the spring-steel stripes. When the structure self-locks, the stiffness experiences a more than 10 time increase (from 0.341 N/mm to 38.7N/mm), which comes from the bending of the facets. Such self-locking induced stiffness jump generates a piecewise stiffness profile of the SSCO structure.

3. DYNAMIC ANALYSIS OF THE SMO STRUCTURE

3.1. Fitted force-displacement profile and equivalent dynamic model

Based on the force-displacement curve obtained in the static test, a third-order polynomial is applied to approximate this curve. Note that the stable equilibria, which correspond to u_1 and u_2, and the unstable equilibrium, which corresponds to

u_0, are of great significance to the structure. Hence we use the following polynomial for curve fitting,

$$F(u) = \alpha(u-u_0)(u-u_1)(u-u_2),$$

where $u_0 = 0$, $u_1 = -14.43mm$, $u_2 = 27.75mm$ according to the static tests (Figure 4). Another point, u_3, corresponding to the maximum negative force, is also used to determine the coefficient $\alpha = 0.0001578\ [10^3 kg/(mm \cdot s)^2]$. Hence the force-displacement profile gives

$$F(u) = 0.0001578u(u+14.43)(u-27.75). \quad (5)$$

The fitted force-displacement profile is also plotted in Figure 4 in dash. Between the two stable configurations, the fitted profile agrees well with the measured curve, while there are some discrepancies when the displacement is far away from the stable configurations. Such discrepancies can be fixed by adopting higher order terms for fitting, while this will add complexity for analysis.

With the fitted force-displacement profile, we are able to study the dynamics of the SMO structure by simplifying it into a nonlinear spring mass system, see Figure 6. Its equation of motion yields

$$\begin{aligned} &m\ddot{u} + F(u) + c\dot{u} = -m\ddot{y}, \\ &u = x - y. \end{aligned} \quad (6)$$

Here x and y denote the absolute displacement of the lumped mass m and the base, respectively; u denotes the relative displacement between the mass and the base, with $u = 0$ being the unstable equilibrium; c is the viscous damping coefficient. The damping mainly comes from the crease made of plastic films. Note that since the force-displacement profile is obtained by fitting the measured curve, it largely preserves the folding properties of the origami prototype.

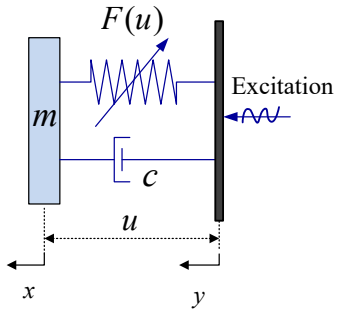

FIGURE 6. Equivalent nonlinear spring mass model of the SMO structure.

3.2. Numerical simulations

To understand the bistable SMO structure's dynamics, numerical simulation is carried out on Eq. (6) with the following parameters: $m = 0.12$kg, $c = 0.6$kg/s. The base is subjected to a harmonic excitation $y = b\sin\omega t$ with amplitude $b = 6$mm and frequency ω. With a step of 0.1 Hz, a discrete frequency sweep is performed between 2 and 20 Hz. In order to capture different dynamics, three initial conditions are applied to the system at each frequency: (-14.43, 0), (0,0), and (27.75, 0). Simulations show that the system is able to produce four types of responses. The intrawell (in) response oscillates around the (-14.43, 0) equilibrium, e.g., at 9.6Hz, see the solid curve in Figure 7(b); the intrawell (out) response oscillates around the (27.75, 0) equilibrium, e.g., at 13 Hz, see the solid curve in Figure 7(c); the periodic interwell response that oscillates around the three equilibria, e.g., at 13 Hz, see the dotted curve in Figure 7(c); and the chaotic interwell response that randomly oscillate around the three equilibria, e.g., at 9.6Hz, see the dotted curve in Figure 7(b).

Considering the possible nonlinear responses, we use root mean squared (RMS) value of the displacement data to characterize the average vibration energy. In addition, we divide the RMS of the lumped mass's steady-state displacement by the RMS of the shaker's excitation displacement to get the displacement transmissibility of the SMO structure in terms of the RMS value, i.e.,

$$T_{\text{d\_RMS}} = \frac{X_{\text{RMS}}}{Y_{\text{RMS}}} = \frac{\sqrt{(x_1^2 + x_2^2 + \ldots + x_N^2)/N}}{\sqrt{(y_1^2 + y_2^2 + \ldots + y_N^2)/N}} \quad (7)$$

The subscript of x and y represents the data points in the simulated displacement time-histories. Figure 7(a) plots the relationship between $T_{\text{d\_RMS}}$ and the excitation frequency. It reveals that in the intrawell responses, the base excitations could be significantly attenuated at relatively high frequency, while the interwell responses have obvious amplification effects.

3.3 Spectrum analyses

While RMS transmissibility provides an insight of the system's performance from an energy point of view, we perform spectrum analyses on the dynamic responses to get more details on the effects of nonlinearity. By applying fast Fourier transform (FFT) on system's responses, we derive the displacement transmissibility of the main frequency components, shown in Figure 7(d). Here the transmissibility is defined as the ratio between the amplitude of main frequency component and that of the base excitation, i.e.,

$$T_{d_k} = \frac{\bar{X}_k}{\bar{Y}_0}, \quad (8)$$

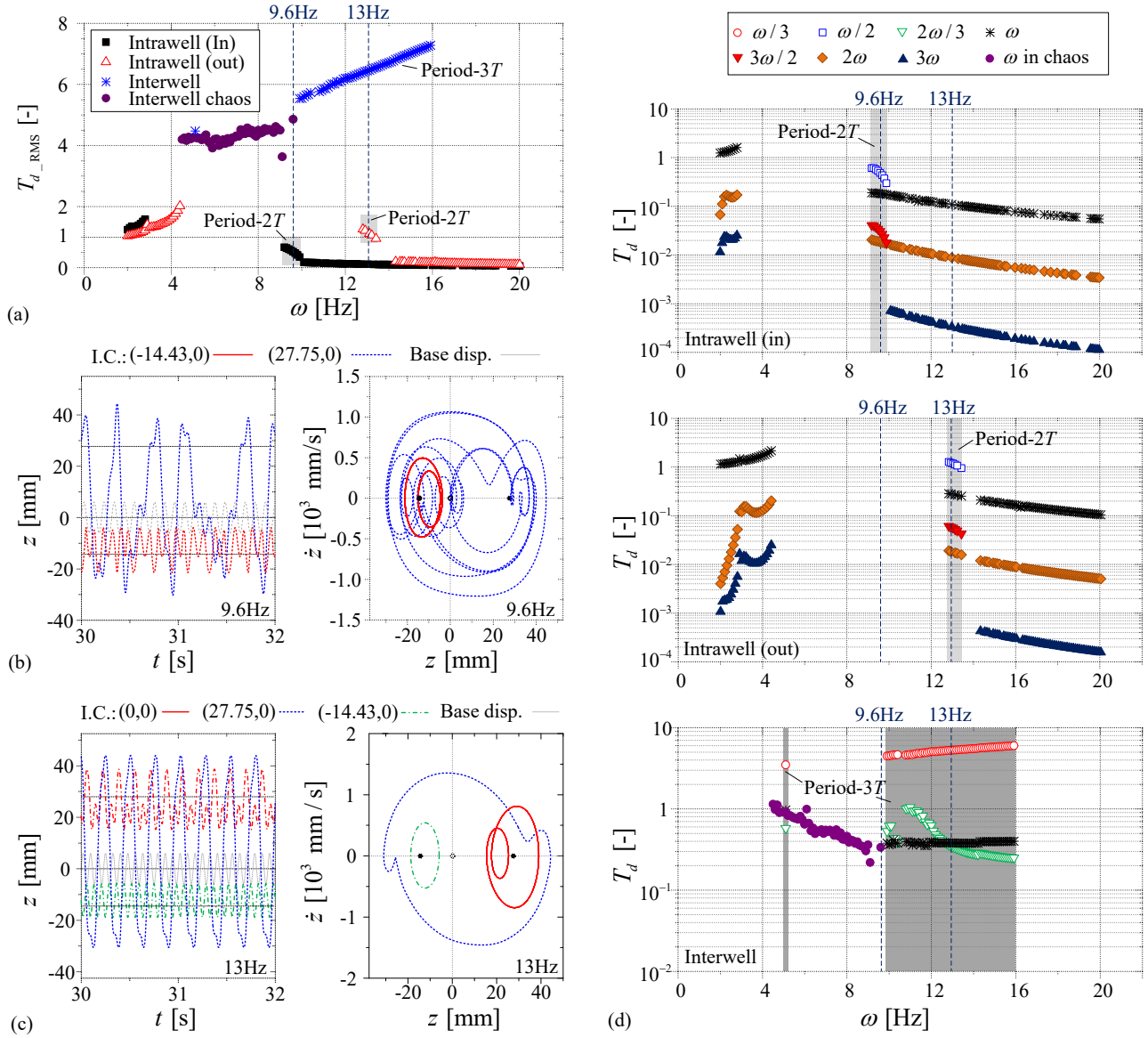

FIGURE 7. Simulation results of the simplified SMO structure. (a) Displacement transimissibility in terms of the RMS value with respect to the excitation frequency. (b) The intrawell (in) (solid) and chaotic interwell (dotted) responses at 9.6 Hz. (c) The intrawell (in) (dash-dotted), intrawell (out) (solid), and periodic interwell (dotted) responses at 13Hz. The different responses are shown in displacement time-histories and phase diagram, and for reference, the excitation signal is also ploteed. (d) From top to bottom, showing the displacement transmissibility of the main frequency components for the intrawell (in), intrawell (out), and interwell responses, respectively.

where $\bar{X}_k$ denote the main frequency component at frequency ω_k, and $\bar{Y}_0$ denote the base excitation amplitude. The results indicate that for the periodic intrawell oscillations, the ω and 2ω components play a leading role; for 2T subharmonic intrawell oscillations, the $\omega/2$, ω, and $3\omega/2$ components dominate; and for 3T subharmonic interwell responses, the $\omega/3$, $2\omega/3$, and ω components govern the oscillations. Such findings indicate that for small-amplitude intra-well oscillations, the quadratic nonlinearity play the main role, while for large-amplitude interwell oscillation, the cubic nonlinearity is more dominant [35].

4. DYNAMIC ANALYSIS OF THE SSCO STRUCTURE

4.1. Fitted force-displacement profile and equivalent dynamic model

Static tests and linear regression show that the SSCO structure possesses a piecewise stiffness profile with two constant stiffness segments. However, only compression tests

are carried out during the experiment, although the SSCO prototype can also be stretched from the stress-free configuration under tensile force. At the initial tension stage, the SSCO prototype remains foldable under tensile force, and shows relatively low stiffness that originates from the bending stiffness of the spring-steel stripes. When the prototype is extended to the configuration that the bottom cell is flat (i.e., $\theta_{A1}=0$), the prototype cannot be further folded to achieve any extension; if keep applying tensile force, the plastic film at the creases will be stretched, generating another stiffness jump. Therefore, the SSCO prototype's overall piecewise stiffness profile consists of three segments, one low stiffness segment during folding, one locking-induced high stiffness segment, and one stretching-induced high stiffness segment.

Figure 8(a) shows the deformation of the SSCO structure. The structure will experience a Δ_2 deformation between the fully-stretched configuration and the stress-free configuration, and a Δ_3 deformation between the stress-free configuration and the locked configuration. With the stiffness profile, we can simplify the SSCO structure into a single DOF lumped-mass system with piecewise stiffness springs (Figure 8(b)). Here the equivalent stiffness and equivalent viscous damping coefficients are given (Figure 8(c)).

$$F(z)=\begin{cases}k_1+\Delta k_3, & \Delta_3<z,\\ k_1, & -\Delta_2<z<\Delta_3,\\ k_1+\Delta k_2, & z<-\Delta_2.\end{cases}$$
$$C(z)=\begin{cases}c_1+\Delta c_3, & \Delta_3<z,\\ c_1, & -\Delta_2<z<\Delta_3,\\ c_1+\Delta c_2, & z<-\Delta_2.\end{cases} \tag{9}$$

Here , x and y indicate the absolute displacements of the lumped mass and the base, respectively, and z denotes the relative displacement between them, i.e., $z=x-y$. Hence, the equation of motion of the SSCO structure under harmonic base excitation can be expressed as

$$\begin{cases}m\ddot{x}+(k_1+\Delta k_3)(x-y)+(c_1+\Delta c_3)(\dot{x}-\dot{y})\\ \qquad =(k_1+\Delta k_3)\Delta_3, & \Delta_3<z,\\ m\ddot{x}+k_1(x-y)+c_1(\dot{x}-\dot{y})=0, & -\Delta_2<z<\Delta_3,\\ m\ddot{x}+(k_1+\Delta k_2)(x-y)+(c_1+\Delta c_2)(\dot{x}-\dot{y})\\ \qquad =-(k_1+\Delta k_2)\Delta_2, & z<-\Delta_2,\end{cases} \tag{10}$$

where $y=Y\sin(\omega t)$ is the harmonic base excitation with amplitude Y and frequency ω.

Introducing the following new parameters

$$\omega_1^2=\frac{k_1}{m},\quad \omega_2^2=\frac{\Delta k_2}{m},\quad \omega_3^2=\frac{\Delta k_3}{m},$$
$$2\xi_1\omega_1=\frac{c_1}{m},\quad 2\xi_2\omega_2=\frac{\Delta c_2}{m},\quad 2\xi_3\omega_3=\frac{\Delta c_3}{m}, \tag{11}$$

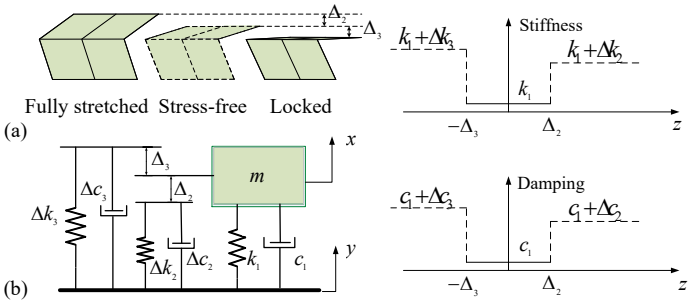

FIGURE 8. (a) Three configurations of SSCO structure: fully stratched, stress-free, and locked configurations. (b) Simplified lumped-mass model of SSCO structure. (c) Equivalent piecewise stiffness and equivalent piecewise viscos damping profilies.

Eq. (10) can be rewritten as

$$\begin{cases}\ddot{z}+\omega_1^2 z+2\xi_1\omega_1\dot{z}=-\ddot{y}, & -\Delta_2<z<\Delta_3,\\ \ddot{z}+(\omega_1^2+\omega_3^2)z+(2\xi_1\omega_1+2\xi_3\omega_3)=\omega_3^2\Delta_3-\ddot{y}, & \Delta_3<z,\\ \ddot{z}+(\omega_1^2+\omega_2^2)z+(2\xi_1\omega_1+2\xi_2\omega_2)=-\omega_2^2\Delta_2-\ddot{y}, & z<-\Delta_2.\end{cases} \tag{12}$$

By utilizing the following relations

$$\begin{aligned}&u=x/Y,\ \ v=y/Y,\ \ w=u-v,\\ &\delta_2=\Delta_2/Y,\ \ \delta_3=\Delta_3/Y,\\ &\square'=\frac{d\square}{d\tau}=\frac{1}{\omega_1}\frac{d\square}{dt},\\ &r=\omega/\omega_1,\ \ \rho_2=\omega_2/\omega_1,\ \ \rho_3=\omega_3/\omega_1,\end{aligned} \tag{13}$$

where Y and ω_1 are the characteristic length and frequency for non-dimensionalization, Eq. (14) can be written in dimensionless from

$$w''+w+2\xi_1 w'=-\ddot{v}+g(w,w'),$$
$$g(w,w')=\begin{cases}-2\rho_3\xi_3 w'-\rho_3^2 w+\rho_3^2\delta_3, & \delta_3<w,\\ 0, & -\delta_2<w<\delta_3,\\ -2\rho_2\xi_2 w'-\rho_2^2 w-\rho_2^2\delta_2, & w<-\delta_2.\end{cases} \tag{14}$$

4.2. Dynamical analysis

Considering that piecewise stiffness is a kind of strong nonlinearity, in this subsection we use the method of averaging to solve Eq. (14) to analyze the dynamics. We assume that the solution of w has the following form

$$\begin{aligned}&w=a(\tau)\sin(r\tau+\beta(\tau)),\\ &w'=a(\tau)r\cos(r\tau+\beta(\tau)),\\ &r\tau+\beta(\tau)=\varphi(\tau).\end{aligned} \tag{15}$$

Differentiating the first equation of (15) with respect to τ, one can eliminate the second equation of (15) and obtain

$$a'\sin(\varphi)+a\beta'\cos(\varphi)=0. \tag{16}$$

Differentiating the second equation of (15) and substituting it into Eq. (14) yields

$$\begin{aligned}&(a'r\cos(\varphi)-a\beta'r\sin(\varphi)-ar^2\sin(\varphi))\\&+2\xi_1(ar\cos(\varphi))+a\sin(\varphi)=r^2\sin(rt)+g(a,\beta),\\&g(a,\beta)=g(w,w')=g(a\sin(\varphi),ar\cos(\varphi)).\end{aligned} \tag{17}$$

Solving Eq. (16) and (17), we have

$$\begin{cases}a'r=\cos(\varphi)[-v''+g(a,\beta)-a\sin(\varphi)\\\qquad\qquad -2\xi_1 ar\cos(\varphi)+ar^2\sin(\varphi)],\\ \beta'ar=-\sin(\varphi)[-v''+g(a,\beta)-a\sin(\varphi)\\\qquad\qquad -2\xi_1 ar\cos(\varphi)+ar^2\sin(\varphi)].\end{cases} \tag{18}$$

In the steady state, the relative displacement w is constant "on the average" with periodic oscillation imposed on. In other words, the variables a and β vary slowly with time in steady state. We integrate and average the right-hand side of Eq. (18) with respect to the fast variable τ from 0 to 2π, which yields two transcendental equations, from which the amplitude-frequency relationship can be obtained.

Table 1 lists the parameters we extract from the static tests, as well as the excitation amplitude and frequency. Based on these parameters, we obtain the displacement transmissibility in terms of the RMS value and plot it in Figure 9. It shows that the system is able to generate two branches of responses. When the excitation frequency is relatively low, the system's response coincides exactly with the corresponding linear system (i.e., with only k_1 and c_1). This is reasonable because under low excitation frequency and amplitude, the relative displacement of the SSCO structure is smaller than Δ_2 or Δ_3 such that locking or over-stretching does not happen, and the system

Table 1. Parameters of SSCO structure.

Parameters	Values
m	0.13g
k_1	0.341×10^3(N/m)
$k_1+\Delta k_2$	38.7×10^3 (N/m)
$k_1+\Delta k_3$	80×10^3 (N/m)
c_1	0.1(N·s/m)
Δc_2, Δc_3	0(N·s/m)
Δ_2, Δ_3	7.5×10^{-3} (m)
Y	15×10^{-3} (m)
ω	2:0.01:30(Hz)

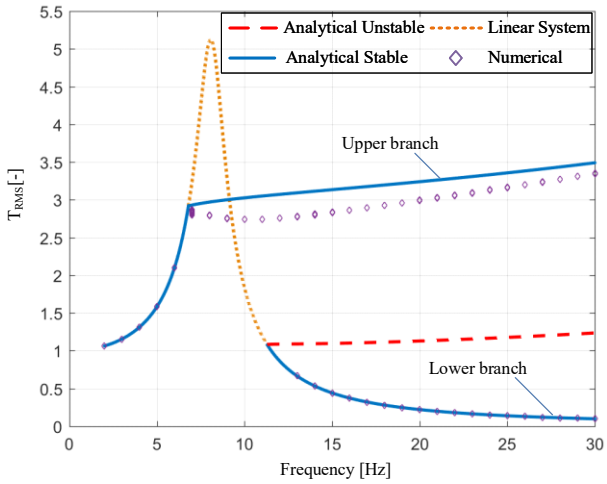

FIGURE 9. Analytical and numerical responses of the simplified SSCO structures.

behaves as the corresponding linear system. However, with the increase of the excitation frequency, the responses no longer coincide with the linear system but bifurcate into two branches. The lower branch, again, behave exactly the same as the corresponding linear system because locking or over-stretching is not triggered. While the upper branch exhibits a hardening nonlinearity characteristics; the displacement transmissibility is much higher than the linear system, because the relative oscillation's amplitude is larger than Δ_2 and Δ_3 such that locking and over-stretching happen during the process.

To verify the correctness of the analytical results, numerical simulations are also carried out on Eq. (14). The obtained displacement transmissibility is plotted in Figure 9 with empty diamond. It shows that the numerical and analytical results agree well with each other, manifesting the correctness of the analytical approach.

5. CONCLUSIONS

Considering that origami-based mechanical metamaterials can be used in a dynamic environment, this research focuses on the dynamic characteristics of origami structures. Two origami structures, namely, the SMO and SSCO are explored in this study. By assigning folding stiffness through pre-bent spring-steel stripes, the SMO structure exhibits obvious structural bistability, and the SSCO structure shows a locking-induced piecewise stiffness profile. Static tests on the SMO and SSCO prototypes give rise to the force-displacement curves, from which, analytical force-displacement or stiffness profiles can be approximated. Based on these profiles, equivalent lumped-mass models can be established. Such models largely capture the folding characteristics of the origami structures.

We then use numerical and analytical approaches to analyze their dynamic responses. In the SMO structure, multiple types of responses are observed, including periodic intrawell

oscillation, subharmonic intrawell oscillations, periodic interwell oscillations, and chaotic interwell oscillations. Spectrum analyses reveal that it is the quadratic and cubic nonlinearities that give rise to these rich dynamics. In the SSCO structure, two branches of responses are observed. One branch corresponds to small amplitude and coincides with the corresponding linear system, because locking or over-stretching does not happen. The other branch of responses exhibits large amplitude and hard nonlinearity characteristics, due to locking and over-stretching during the excitation.

The results of this research offer a wealth of fundamental insights into the dynamics of origami folding, and provide a solid foundation for developing foldable and deployable structures and mechanical metamaterials with embedded dynamic functionalities.

ACKNOWLEDGMENTS

This research was partially supported by the National Science Foundation under Award 1634545 and the University of Michigan Collegiate Professorship.

REFERENCES

[1] Marras, A. E., Zhou, L., Su, H.-J., and Castro, C. E., 2015, "Programmable motion of DNA origami mechanisms TL - 112," Proc. Natl. Acad. Sci., **112 VN**-(3), pp. 713–718.

[2] Randall, C. L., Gultepe, E., and Gracias, D. H., 2012, "Self-folding devices and materials for biomedical applications," Trends Biotechnol., **30**(3), pp. 138–146.

[3] Kuribayashi, K., Tsuchiya, K., You, Z., Tomus, D., Umemoto, M., Ito, T., and Sasaki, M., 2006, "Self-deployable origami stent grafts as a biomedical application of Ni-rich TiNi shape memory alloy foil," Mater. Sci. Eng. A, **419**(1–2), pp. 131–137.

[4] Peraza-Hernandez, E. A., Hartl, D. J., Malak Jr, R. J., and Lagoudas, D. C., 2014, "Origami-inspired active structures: a synthesis and review," Smart Mater. Struct., **23**(9), p. 94001.

[5] Felton, S., Tolley, M., Demaine, E., Rus, D., and Wood, R., 2014, "A method for building self-folding machines," Science (80-.)., **345**(6197), pp. 644–646.

[6] Zhakypov, Z., Falahi, M., Shah, M., and Paik, J., 2015, "The design and control of the multi-modal locomotion origami robot, Tribot," Proceedings of the IEEE International Conference on Intelligent Robots and Systems, Hamburg, Germany, pp. 4349–4355.

[7] Fang, H., Zhang, Y., and Wang, K. W., 2017, "An earthworm-like robot using origami-ball structures," Proc. SPIE 10164, Active and Passive Smart Structures and Integrated Systems 2017, p. 1016414.

[8] Gattas, J. M., and You, Z., 2015, "Geometric assembly of rigid-foldable morphing sandwich structures," Eng. Struct., **94**, pp. 149–159.

[9] Martinez, R. V, Fish, C. R., Chen, X., and Whitesides, G. M., 2012, "Elastomeric origami: Programmable paper-elastomer composites as pneumatic actuators," Adv. Funct. Mater., **22**(7), pp. 1376–1384.

[10] Schenk, M., Viquerat, A. D., Seffen, K. a., and Guest, S. D., 2014, "Review of Inflatable Booms for Deployable Space Structures: Packing and Rigidization," J. Spacecr. Rockets, **51**(3), pp. 762–778.

[11] Reis, P. M., López Jiménez, F., and Marthelot, J., 2015, "Transforming architectures inspired by origami," Proc. Natl. Acad. Sci., **112**(40), p. 201516974.

[12] Schenk, M., and Guest, S. D., 2013, "Geometry of Miura-folded metamaterials," Proc. Natl. Acad. Sci., **110**(9), pp. 3276–3281.

[13] Yasuda, H., and Yang, J., 2015, "Reentrant Origami-Based Metamaterials with Negative Poisson's Ratio and Bistability," Phys. Rev. Lett., **114**(18), p. 185502.

[14] Fang, H., Li, S., Ji, H., and Wang, K. W., 2016, "Uncovering the deformation mechanisms of origami metamaterials by introducing generic degree-4 vertices," Phys. Rev. E, **94**(4), p. 43002.

[15] Silverberg, J. L., Evans, A. A., McLeod, L., Hayward, R. C., Hull, T., Santangelo, C. D., and Cohen, I., 2014, "Using origami design principles to fold reprogrammable mechanical metamaterials," Science (80-.)., **345**(6197), pp. 647–650.

[16] Fang, H., Li, S., and Wang, K. W., 2016, "Self-locking degree-4 vertex origami structures," Proc. R. Soc. A Math. Phys. Eng. Sci., **472**(2195), p. 20160682.

[17] Waitukaitis, S., Menaut, R., Chen, B. G., and van Hecke, M., 2015, "Origami Multistability: From Single Vertices to Metasheets," Phys. Rev. Lett., **114**(5), p. 55503.

[18] Li, S., and Wang, K. W., 2015, "Fluidic origami with embedded pressure dependent multi-stability: a plant inspired innovation," J. R. Soc. Interface, **12**(111), p. 20150639.

[19] Filipov, E. T., Tachi, T., and Paulino, G. H., 2015, "Origami tubes assembled into stiff, yet reconfigurable structures and metamaterials.," Proc. Natl. Acad. Sci. U. S. A., **112**(40), pp. 12321–12326.

[20] Li, S., Fang, H., and Wang, K. W., 2016, "Recoverable and programmable collapse from folding pressurized origami cellular solids," Phys. Rev. Lett., **117**(11), p. 114301.

[21] Yasuda, H., Chong, C., Charalampidis, E. G., Kevrekidis, P. G., and Yang, J., 2016, "Formation of rarefaction waves in origami-based metamaterials," Phys. Rev. E - Stat. Nonlinear, Soft Matter Phys., **93**(4), pp. 1–11.

[22] Yasuda, H., Lee, M., and Yang, J., 2016, "Tunable Wave Dynamics in Origami-Based Mechanical Metamaterials," Proceedings of the ASME 2016 International Design Engineering Technical

Conferences and Computers and Information in Engineering Conference, p. DETC2016-59592.
[23] Ishida, S., Suzuki, K., and Shimosaka, H., 2016, "Design and Experimental Analysis of Origami-Inspired Vibration Isolators With Quasi-Zero-Stiffness Characteristic," Proceedings of the ASME 2016 International Design Engineering Technical Conferences and Computers and Information in Engineering Conference, p. DETC2016-59699.
[24] Li, S., and Wang, K. W., 2015, "Fluidic origami cellular structure – Combining the plant nastic movements with paper folding art," Proc. SPIE 9431, Active and Passive Smart Structures and Integrated Systems 2015, W.-H. Liao, G. Park, and A. Erturk, eds., SPIE, San Diego, CA, p. 94310H.
[25] Harne, R. L., and Wang, K. W., 2017, Harnessing Bistable Structural Dynamics – for Vibration Control, Energy Harvesting, and Sensing, John Wiley and Sons.
[26] Harne, R. L., and Wang, K. W., 2013, "A review of the recent research on vibration energy harvesting via bistable systems," Smart Mater. Struct., **22**(2), p. 23001.
[27] Gerson, Y., Krylov, S., Ilic, B., and Schreiber, D., 2012, "Design considerations of a large-displacement multistable micro actuator with serially connected bistable elements," Finite Elem. Anal. Des., **49**(1), pp. 58–69.
[28] Fang, H., and Wang, K. W., 2017, "Piezoelectric vibration-driven locomotion systems – Exploiting resonance and bistable dynamics," J. Sound Vib., **391**, pp. 153–169.
[29] Yang, K., Harne, R. L., Wang, K. W., and Huang, H., 2014, "Investigation of a bistable dual-stage vibration isolator under harmonic excitation," Smart Mater. Struct., **23**(4), p. 45033.
[30] Waitukaitis, S., and van Hecke, M., 2016, "Origami building blocks: generic and special 4-vertices," Phys. Rev. E, **93**(2), p. 23003.
[31] Leong, T. G., Lester, P. A., Koh, T. L., Call, E. K., and Gracias, D. H., 2007, "Surface Tension-Driven Self-Folding Polyhedra," Langmuir, **23**(17), pp. 8747–8751.
[32] Felton, S. M., Tolley, M. T., Shin, B., Onal, C. D., Demaine, E. D., Rus, D., and Wood, R. J., 2013, "Self-folding with shape memory composites," Soft Matter, **9**(32), pp. 7688–7694.
[33] Running, D. M., Ligon, J. B., and Miskioglu, I., 2004, "Frequency response of a piecewise linear vibration isolator," J. Vib. Control, **10**(12), pp. 1775–1794.
[34] Pun, D., and Liu, Y. B., 2000, "On the Design of the Piecewise Linear Vibration Absorber," Nonlinear Dyn., **22**(4), pp. 393–413.
[35] Fang, H., Li, S., Ji, H., and Wang, K. W., 2017, "Dynamics of a bistable Miura-origami structure," Phys. Rev. E, **95**(5), p. 52211.